Activation and Monitoring of mtDNA Damage in Cancer Cells *via* the "Proton-Triggered" Decomposition of an Ultrathin Nanosheet

*Jun W. Liu,[1,‡] Yong G. Yang,[1,‡] Kui Wang,[1] Ge Wang,[3] Cong C. Shen,[1] Yue H. Chen,[1] Yu F. Liu,[1] Tony D. James,[2] Kai Jiang,[1] and Hua Zhang[1,]**

[1]Key Laboratory of Green Chemical Media and Reactions, Ministry of Education; School of Chemistry and Chemical Engineering; School of Physics; School of environment; Henan Normal University, Xinxiang, Henan 453007, China

[2]Department of Chemistry, University of Bath, Bath, BA2 7AY, UK

[3]School of Basic Medical Sciences, Xinxiang Medical University, Xinxiang, Henan 453003, China

KEYWORDS: Proton-triggered, hydroxyapatite, ultrathin nanosheet, mtDNA damage, cancer cell

ABSTRACT: Mitochondrial DNA (mtDNA) damage is a very important molecular event, which has significant effects on living organisms. Therefore, a particularly important challenge for biomaterials research is to develop functionalized nanoparticles that can activate and monitor mtDNA damage and instigate cancer cell apoptosis, and as such eliminate the negative effects on living organisms. Towards that goal, with this research we have developed a hydroxyapatite

ultrathin nanosheet (**HAP-PDCns**)—a high Ca^{2+} content biomaterial. **HAP-PDCns** undergoes proton-triggered decomposition after entering cancer cells *via* clathrin-mediated endocytosis, and then, it selectively concentrates in the charged mitochondrial membrane. This kind of proton-triggered decomposition phenomenon facilitates mtDNA damage by causing instantaneous local calcium overload in the mitochondria of cancer cells, and inhibits tumor growth. Importantly, at the same time, a real-time green-red-green fluorescence change occurs that correlates with the degree of mtDNA deterioration, due to changes in HOMO-LUMO energy gaps during this process. Significantly, the decomposition and the fluorescence changes cannot be triggered in normal cells. Thus, **HAP-PDCns** can selectively induce apoptosis and the death of a cancer cell by facilitating mtDNA damage, but does not affect normal cells. In addition, **HAP-PDCns** can simultaneously monitor the degree of mtDNA damage. We anticipate that this design strategy can be generalized to develop other functionalized biomaterials that can be used to instigate the positive effects of mtDNA damage on living organisms whilst eliminating any negative effects.

INTRODUCTION

Mitochondrial DNA (mtDNA) is the special genetic material associated with the mitochondrion.[1-3] mtDNA possesses a unique structural characteristic—an extremely small double-stranded circular structure.[1,2] In addition, it possesses unique functional characteristics that other genetic material does not, which is only carried through to subsequent generations by maternal inheritance.[1,3] As a result of these special structural and functional characteristics, mtDNA plays unique roles in the processes associated with the development of cancer, such as proliferation, apoptosis etc.[2-5] More importantly, on account of the lack of introne and histone protection, mtDNA exhibits a > 10-fold higher rate of damage than that of nuclear DNA.[6,7]

Therefore, mtDNA is more prone to damage when nanoparticles cause an imbalance of endogenous factors (including reactive oxygen species and ions) which can be generated by nanoparticles when they enter living cells. As a result of the imbalances, different types of damage can occur, for example, substitution, deletion, insertion, exon skipping etc.[8,9] Furthermore, because there is no DNA damage repair system in the mitochondria, once mtDNA damage occurs, it cannot be repaired, which results in permanent structural changes in the mtDNA and gene mutation.[10,11] When mtDNA mutates (up to 60%) within a very short period of time, mtDNA damage can cause several important effects on different living organisms.[12,13] For example, mtDNA damage can inhibit cancer cell division which results in slower tumor growth and reduced proliferation resulting in a positive outcome for the living organism.[14-16] As such, developing nanoparticles that can intelligently induce and in real-time simultaneously monitor mtDNA damage are immensely important, particularly for the development of applied biomaterials for therapeutic applications.[17-23]

How to coordinate the activation and monitoring of nanoparticles for mtDNA damage in real-time is one of the important challenges for the development of applied biomaterials. In recent years, many kinds of nanomaterials have been cultivated and used to induce DNA damage in order to produce a positive therapeutic outcome,[24-28] including nanoparticles,[16, 24,25] WO_{3-x} nanodots,[26] Bi_2Se_3 nanoplates,[27] and so on.[28] After hydroxyapatite-based nanoparticles undergo mediated endocytosis into different cells including cancer cells and normal cells, these bionic materials have many potential applications in the area of applied biomaterials, for example, the activation of DNA damage.[29-34] 1-10 nm hydroxyapatite (100 μg/ml) can cause DNA damage in cells by inducing P53, P21 and HSP70 up-regulation.[29] In addition, hydroxyapatite nanoparticles exposed to alternating magnetic fields can cause DNA damage by increasing the temperature of living cells

over a very short time period.[30] Magnetic hydroxyapatite nanoparticles can induce DNA damage by increasing the concentration of intracellular reactive oxygen species.[31,32] Furthermore, nano-hydroxyapatites substituted with iron, silica and fluorine efficiently facilitate increased DNA damage.[33,34] However, while these systems have successfully induced DNA damage, they are not able to intelligently regulate and report on the level of induced injury. Therefore, highly fluorescent hydroxyapatite nanoparticles have been designed and synthesized by doping with metal ion (such as Tb^{3+}, Er^{3+}, Eu^{3+}, La^{3+}, Dy^{3+}) or dyes.[35-39] Such systems can be used for the fluorescence analysis of solutions, but cannot target and induce mtDNA damage nor facilitate real-time monitoring of mtDNA damage in living cancer cells. Furthermore, the internalization mechanisms of these hydroxyapatites have not been reported, which limits the design of related materials for biological applications, especially for inducing DNA damage. Therefore, the development of intelligent fluorescent hydroxyapatite-nanoprobes that can induce and facilitate real-time monitoring of mtDNA damage in living organisms are urgently required.

With this research we set out to induce and monitor in real-time mtDNA damage and encourage apoptosis and death of living cancer cells using a hydroxyapatite ultrathin nanosheet. The ultrathin nanosheet was doped with pyrazine-2,3-dicarbonitrile (**HAP-PDCns**, **Scheme 1**). To induce mtDNA damage, biomaterials rich in Ca^{2+}—hydroxyapatite were selected as a key component of the **HAP-PDCns**, since they can cause intracellular calcium overload once they fully disintegrate. To improve the efficiency of the material entering tumor cells, the highly efficient clathrin-mediated endocytosis was selected as the target pathway to facilitate designed material entering the organism.[40] Thus, a pyrazine-2,3-dicarbonitrile derivative, 3-((2-(dimethylamino)ethyl)amino)acenaphtho[1,2-*b*]pyrazine-8,9-dicarbonitrile (PDC, **Scheme 1**) that possesses a molecular structure that can specifically target clathrin was introduced into the **HAP-**

PDCns,[41] therefore facilitating the entry of **HAP-PDCns** into cells by clathrin endocytosis. Furthermore, PDC was chosen as a key component (*i.e.* the fluorophore) for **HAP-PDCns** since it facilitates the use of fluorescence for the monitoring of mtDNA damage. These two key components were hybridized using hydrogen bonding to form the loose structured **HAP-PDCns**. Such loose structured **HAP-PDCns** formed by this hybridization process significantly influences the decomposition mechanism. **HAP-PDCns** was prepared using a gentle water-alcohol solvent precipitation method at 37°C in the presence of $Ca(NO_3)_2$ and K_2HPO_4 (pH = 7.4), the morphology and size were evaluated using high resolution transmission electron microscopy (HR-TEM) and X-ray diffraction (XRD) methods. The fluorophore part PDC was prepared and fully characterized and the details are given in the Supporting Information (Scheme S1).

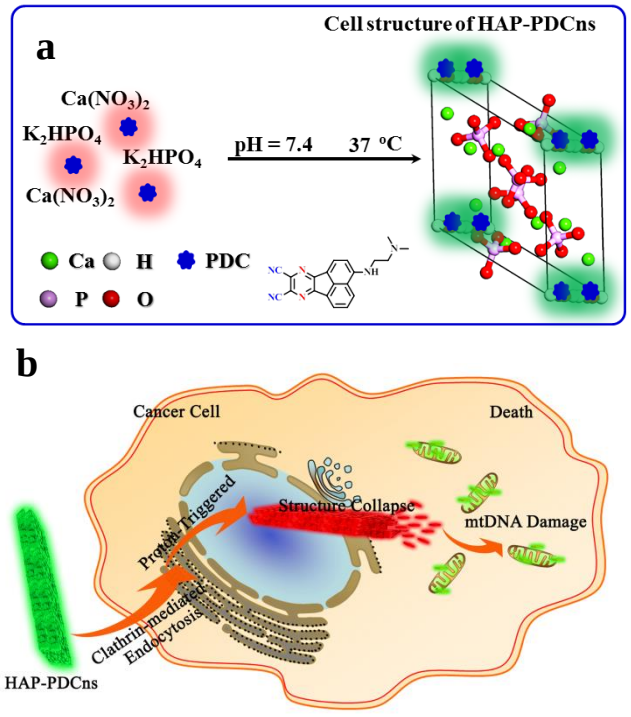

Scheme 1. Schematic preparation of **HAP-PDCns** using a pyrazinedicarbonitrile derivative (a) and the schematic diagram of sensing and anti-cancer mechanisms (b).

RESULTS AND DISCUSSION

The X-ray diffraction spectra (XRD, **Figure 1a**) contains sharp diffraction peaks, confirming the formation of crystals with diffraction peaks corresponding to the planes of the hexagonal **HAP-PDCns** (JCPDF 09-0432), respectively. The unit cell that was obtained from XRD indicated that -OH groups were distributed at each cell vertex (**Scheme 1**), which is favorable for the combination of HAP and PDC. This is clearly evidenced in the emission spectra (**Figure 1b**), where a blue shift (approximately 60 nm) was observed between the spectrum of **HAP-PDCns** and PDC, indicating hydrogen bonding between **HAP-PDCns** and PDC. Furthermore, the infrared spectra indicated that the -OH in **HAP-PDCns** shifts from 3569 cm^{-1} to 3484 cm^{-1} compared with HAP (**Figure 1c**). These results suggest that the dye molecule PDC interacts with HAP by a hydrogen bond between the -OH group in HAP and -CN group in PDC. For morphology and size analysis, HR-TEM (**Figure 1d**) and FE-SEM (**Figure 1e**) indicate that **HAP-PDCns** exits as ultrathin nanosheets with an average thickness of 3.39 ± 0.03 nm (**Figure 1e**, Inset). The physical adsorption (BET, Figure S1 and Table S1) results indicate that the surface area of **HAP-PDCns** is 137 m^2/g, which confirms that **HAP-PDCns** is a loose open structure.[42] A comparison of the classic hydroxyapatite (HAP) with **HAP-PDCns** indicates that the changes in structure can be attributed to the presence of the PDC in the ultrathin nanosheets.

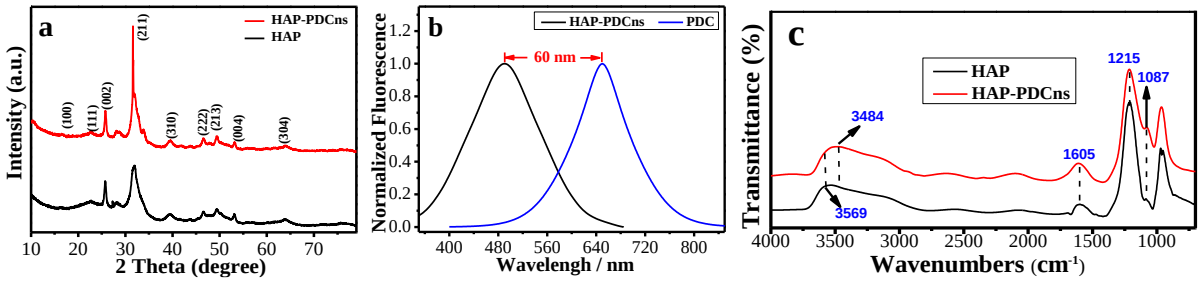

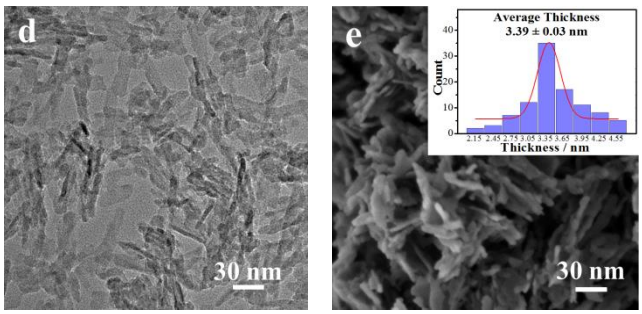

Figure 1. X-ray diffraction spectrum (XRD, a), emission spectra (b), FT-IR diffuse reflectance (c), HR-TEM (d) and FE-SEM (e) of **HAP-PDCns**. The inset graph of (e) is thickness distribution of **HAP-PDCns**.

Firstly, we set out to investigate the ability of **HAP-PDCns** to enter cells and then investigate the specific interactions with mtDNA of living cancer cells. **Figure 2** (I Process) indicated that **HAP-PDCns** can enter either cancer cells (HepG 2 cell line) or normal cells (AML12 cell line) within 30 min, because cancer cells and normal cells both exhibit endocytosis. Furthermore, because the endocytosis levels of all cancer cells are higher than that of normal cells,[43,44] HepG 2 cell line exhibits a stronger fluorescent signal than the AML12 cell line (**Figure 2**, I Process). To verify internalization of the nanoparticles into cells including cancer cells and normal cells, inhibition of endocytosis was used to verify the internalisation of **HAP-PDCns** into cells using microscopic imaging (**Figure 3a** and Figure S2a). The strength histogram (**Figure 3b**) and high throughput data statistics (**Figure 3c**) indicated that the fluorescence intensity of **HAP-PDCns** substantially decreased when compared with the normal experimental group after the clathrin-mediated endocytosis was inhibited using an exclusive inhibitor (20 μM of chlorpromazine for 1.0 h). However, using other inhibitors, including chloroquine phosphate; Beta-cyclodextrin; and amiloride (Figure S2a), for endosome, caveolae and macropinocytosis-mediated endocytosis did not reduce the fluorescence. These results clearly indicate that **HAP-PDCns** selectively enters cells *via* endocytosis mediated by clathrin. Furthermore, the extracted fluorescence spectrum of **Figure 2** (I Process) indicated that **HAP-PDCns** enters cancer cells more efficiently than normal

cells, which is due to the higher levels of endocytosis for cancer cells when compared to normal cells.[43,44]

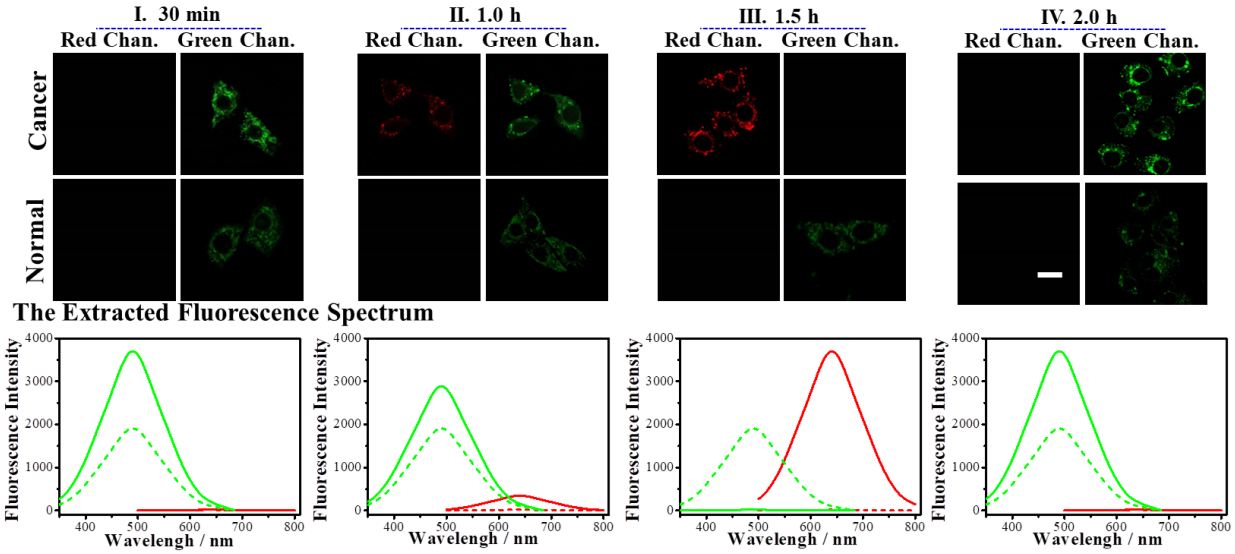

Figure 2. HAP-PDCns (0.40 mg/mL) in cancer cells (HepG 2 cell line) and normal cells (AML12 cells). The extracted fluorescence spectrum was obtained from each imaging result using FV10-ASW. The fluorescence signal collection wavelength: green channel at 490-540 nm, red channel at 620-670 nm, excited at 458 nm. The incubation times are 30 min (I Process), 1.0 h (II Process), 1.5 h (III Process) and 2.0 h (IV Process), respectively. Scale Represents: 15 μm.

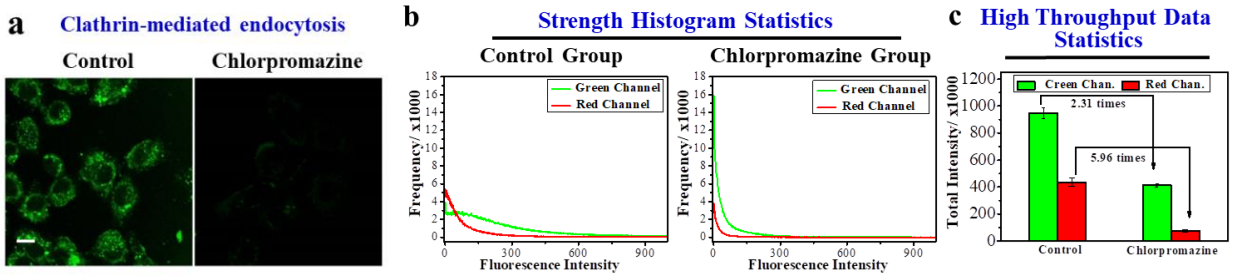

Figure 3. HAP-PDCns (0.20 mg/mL) internalization into cells. (a) The fluorescence signal collection wavelength: green channel at 490-540 nm, red channel at 620-670 nm, excited at 458 nm. The incubation times: 20 μM of chlorpromazine for 1.0 h in HepG 2 cell line; after that, the incubation time of **HAP-PDCns** (0.20

mg/mL is 1.0 h. (b) The strength histogram statistics of green channel and red channel in Figure a. (c) The high throughput data statistics of green channel and red channel in Figure a. The experiments were performed in parallel three times. Scale: 10 μm.

Furthermore, **Figure 2** indicated that **HAP-PDCns** in cancer cells produces obvious regional color rendering with increasing incubation times (1.0 h-II Process, 1.5 h-III Process and 2.0 h-IV Process). Cell morphological analysis (intracellular localization experiment, $R^2 = 0.94$, **Figure 4a**) indicated that **HAP-PDCns** locates in the mitochondria. **Figure 4b** and **Figure S3** demonstrates that the fluorescence intensity of **HAP-PDCns** located in the mitochondria decreases after the mitochondrial membrane potential (MMP) was inhibited (reduced protonation of the membrane) by carbonyl cyanide-m-chlorophenylhydrazone (20 μM for 24 h) and pentobarbital (30 μM for 24 h). The MMP is the main reason for **HAP-PDCns** locating in the mitochondria. Furthermore, agarose gel electrophoresis (**Figure 4c**) indicates that **HAP-PDCns** acts on mtDNA in the mitochondria. To further illustrate the mtDNA targeting of **HAP-PDCns**, mtDNA intracellular digestion was used as a reverse proof. **Figure 4d** clearly indicates that **HAP-PDCns** displays a distinct fluorescence signal with mtDNA of the living cells without DNA digestion enzyme (left microscopic image in **Figure 4d**). However, after the mtDNA was digested by the DNA digestion enzyme, the fluorescence intensity gradually reduces with increasing digestion time, since Ade7 and Gua8 of the mtDNA can no longer interact with the PDC. These results further demonstrate that **HAP-PDCns** targets mtDNA in living cancer cells. The above experiments and data analysis confirm that **HAP-PDCns** is located in the mitochondria of living cancer cells, and **HAP-PDCns** undergoes specific molecular interactions with nucleic acid in the mitochondria—mtDNA.

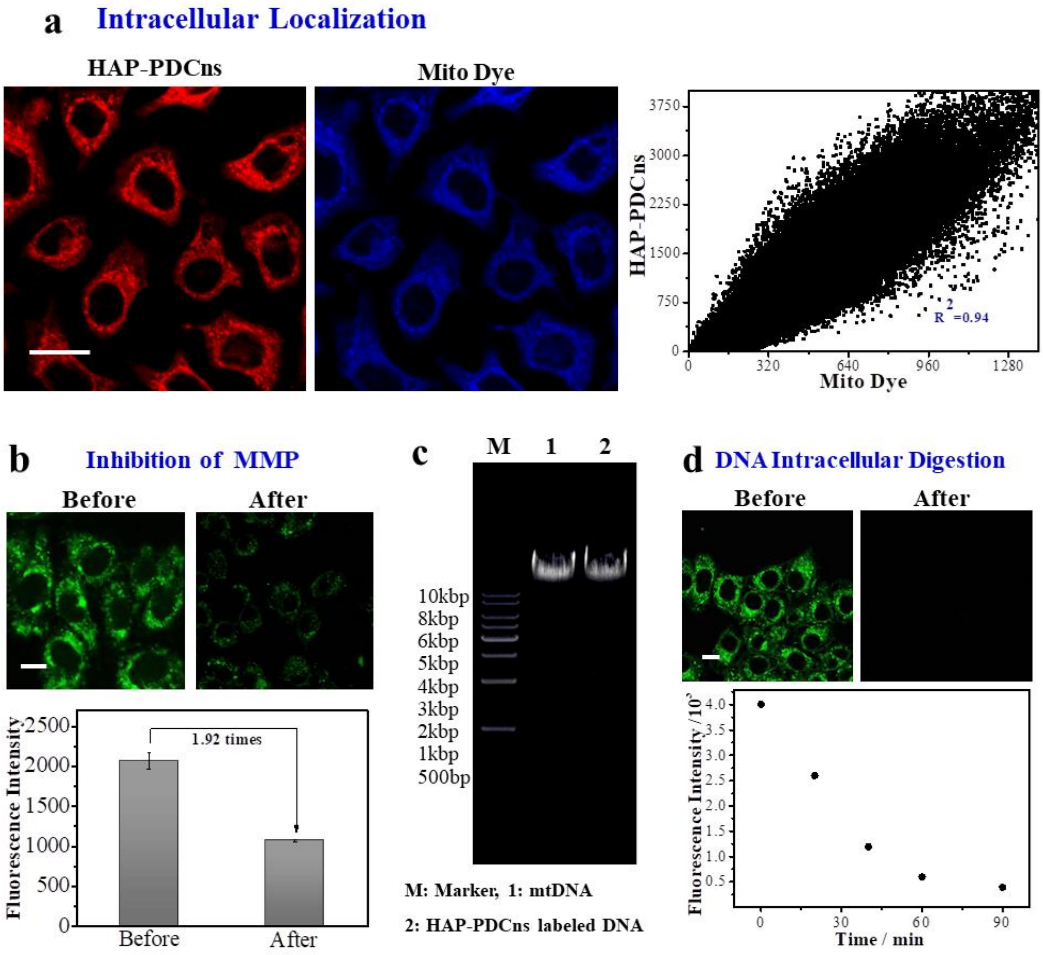

Figure 4. (a) Intracellular localization experiments, **HAP-PDCns** (0.40 mg/mL, emission wavelength: 590-680 nm, excited at 458 nm) and Mito dye (1.0 μM, emission wavelength: 500-540 nm, excited at 488 nm) in cancer cells (HepG 2 cell line). (b) Inhibition of mitochondrial membrane potential (MMP) by carbonyl cyanide-m-chlorophenylhydrazone (20 μM of CCCP for 24 h) in cancer cells (HepG 2 cell line). The experiments were performed in parallel three times. (c) Agarose gel electrophoresis, band 1 (control group): agarose gel electrophoresis of commercial mtDNA; band 2 (experiment group): agarose gel electrophoresis of labeled mtDNA by **HAP-PDCns**. (d) DNA intracellular digestion, DNA digestion enzymes (100 u/mL), digestion time 0-1.5 h. Scale: 10 μm.

We then evaluated how **HAP-PDCns** facilitates mtDNA damage and results in the apoptosis and death of cancer cells, resulting in positive effects for the living organism. Firstly, an MTT

assay (**Figure 5a**) was used to evaluate the effects of **HAP-PDCns** and its components (HAP and PDC) on the viability of cancer cells (HepG 2 cell line) and normal cells (AML12 cell line). **Figure 5a** indicated that there is no significant difference with PDC at different concentrations (5.0 μM and 20.0 μM) for the cell viability with all kinds of living cells. While, HAP at high dosages exhibits inhibition of the cell viability for all kinds of the living cells. However, **HAP-PDCns** can selectively and effectively inhibit the proliferation of cancer cells—HepG 2 cell line over normal cells—AML12 cell line (**Figure 5a**) although **HAP-PDCns** can enter both kinds of cells. More importantly, the IC_{50} values (**Figure 5b**) for **HAP-PDCns** towards cancer cells is 0.028 mg/mL, while an IC_{50} values for **HAP-PDCns** towards AML12 cells could not be detected. These results indicate that **HAP-PDCns** at very low dosages exhibits remarkable anti-proliferation effects on cancer cells, but, negligible effects on normal cells. To prove that this effect was caused by DNA damage, single cell gel electrophoresis (comet assay, **Figure 5c**) was used to evaluate the degree of DNA damage. The mtDNA damage rate of cancer cells at 30 min was negligible. With an increase in incubation time, the damage rate of cancer cells gradually and gently increases. While cancer cells exhibited a slight trailing phenomenon (**Figure 5c**), and the tail length was 5.43 ± 1.73 μm when the incubation time was 1.5 h (Table S2). However, the damage rate of cancer cells exhibited significant changes over the next half hour. At 2.0 h, the mtDNA damage rate of the cancer cells sharply increased to about 90% (**Figure 5c**) and the trailing phenomenon of the damaged cancer cells becomes more significant. The tail length increases to 50.43 ± 12.79 μm (Table S2). Flow cytometry data indicated that about 60% of the cancer cells have entered apoptosis or are dead (**Figure 5c** and Figure S4). However, **HAP-PDCns** did not induce the same effect on normal cells, even though **HAP-PDCns** can enter normal cells. Subsequently, the effect of **HAP-PDCns** was verified *in vivo* (**Figure 5d-5f**). Tumor-bearing (S180 cell line) BALB/c mice were injected with **HAP-PDCns** (Dosage: 0.40 mg/mL), HAP (Dosage: 0.40 mg/mL) and PDC (Dosage: 5.0 μM) continuously for 15 d, respectively. The results (**Figure 5d** and **Figure 5e**)

indicate a significant decrease in tumor size after treatment by **HAP-PDCns** at low dosages (0.0004 mg/mL) compared with the control, HAP and PDC groups, respectively. In addition, tumor volume changes in **Figure 5d** are particularly conspicuous (comparing tumor volume (V) with the original tumor volume (V_0)). Since, V/V_0 of control group and PDC group sharply increase to 4.6 and 4.9, respectively. While, the experimental group treated with HAP (0.40 mg/mL) increases by up to 3.9. However, V/V_0 decreases to 0.84 by the injection only 0.0004 mg/mL of **HAP-PDCns** and, there is an even bigger decrease of V/V_0 to about 0.47 when the injection concentration is 0.40 mg/mL. These results indicate that **HAP-PDCns** exhibits significant curbing effects for tumor growth *in vivo*, compared with HAP and PDC. Moreover, the clinicopathological analysis (**Figure 5f**) using hematoxylin and eosin (H&E)-staining indicates a large area of damage after treatment with **HAP-PDCns**. However, only a small region was damaged when exposed to HAP, and, almost no damage was observed with PDC and saline solution (the blank control group). These results obtained by the clinicopathological analysis confirm that **HAP-PDCns** produces a significant positive effect for halting the advancement of cancer *in vivo*.

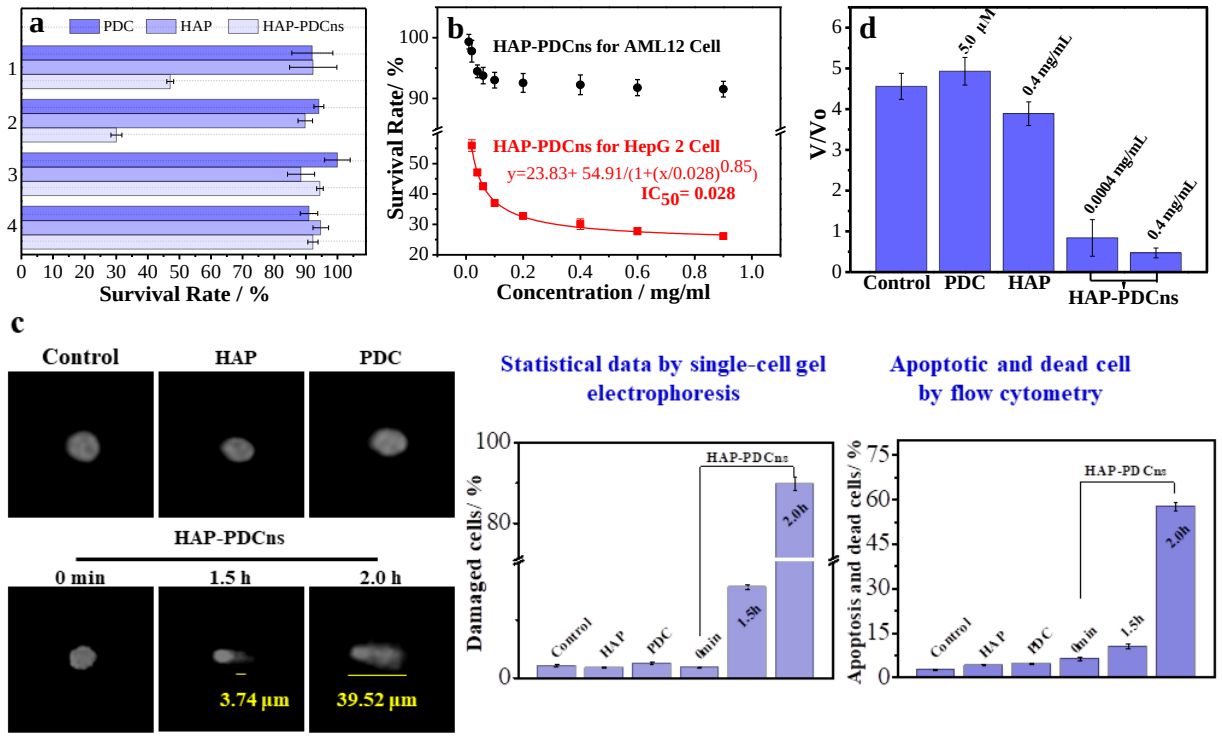

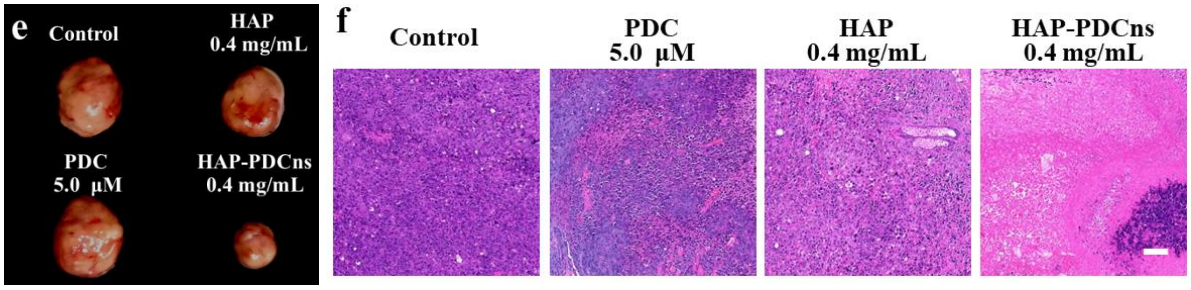

Figure 5. The positive effects of **HAP-PDCns** for cancer therapy. (a) The survival rate of live cells incubated with PDC, HAP and **HAP-PDCns** for 24 h. 1. HepG 2 cell line, PDC: 5.0 μM, HAP and **HAP-PDCns**: 0.04 mg/mL; 2. HepG 2 cell line, PDC: 20.0 μM, HAP and **HAP-PDCns**: 0.40 mg/mL; 3. AML12 cell lines, PDC: 5.0 μM, HAP and **HAP-PDCns**: 0.04 mg/mL; 4. AML12 cell lines, PDC: 20.0 μM, HAP and **HAP-PDCns**: 0.40 mg/mL. The experiments were performed in parallel three times. (b) The IC_{50} of **HAP-PDCns** for HepG 2 cells and AML12 cells. (c) The cell damage imaging and damage degree statistical data by single-cell gel electrophoresis, apoptosis and dead cells by flow cytometry, **HAP-PDCns** (0.40 mg/mL) PDC (5.0 μM) and HAP (0.40 mg/mL). The experiments were performed in parallel three times. (d) The tumor volume change, tumor-bearing (S180 cell line) BALB/c mice were injected with **HAP-PDCns** (Dosage: 0.0004 mg/mL and 0.40 mg/mL), HAP (Dosage: 0.40 mg/mL) and PDC (Dosage: 5.0 μM) continuously for 15 d by intratumoral injection, respectively. The dates were obtained in parallel three times. (e) The visual images of tumor volume change, tumor-bearing (S180 cell line) BALB/c mice were injected with **HAP-PDCns** (Dosage: 0.40 mg/mL), HAP (Dosage: 0.40 mg/mL) and PDC (Dosage: 5.0 μM) continuously for 15 d by intratumoral injection, respectively. (f) The clinicopathological analysis using hematoxylin and eosin (H&E)-staining. Scale: 100 μm.

In addition, **HAP-PDCns** ehibits an intelligent monitoring capability for mtDNA damage during the whole process (**Figure 2**). **Figure 2 I Process** showed that **HAP-PDCns** emits a green fluorescence signal at 490-550 nm in cancer cells when they were incubated with 0.40 mg/mL of **HAP-PDCns** for 30 min. Then the green fluorescence gradually decreases, and a red fluorescence (peak at 640 nm) appears and its intensity increases with increasing incubation time (30 min-1.5 h, **Figure 2 II Process** and **Figure 2 III Process**), that is for the situation involving slight mtDNA damage. After 1.5 h, the green fluorescence signal disappears and the red fluorescence intensity

reaches a maximum (**Figure 2 III Process**). When the mtDNA damage sharply increases to about 90% (2.0 h, **Figure 5c**), at this point the monitoring signal—the red fluorescence intensity dissapears and the green fluorescence signal reappears (**Figure 2 IV Process**). Such green-red-green monitoring signal changes with **HAP-PDCns** can help monitor the level of mtDNA damage, and could be used to monitor cancer cell apoptosis and death. However, the monitoring ability of **HAP-PDCns** does not occur with normal cells (**Figure 2**). Therefore, **HAP-PDCns** displays excellent activation and monitoring performance for mtDNA damage specifically in cancer cells, but not for normal cells. Furthermore, the two main components of **HAP-PDCns**, PDC (**Figure 5c** and Figure S2b) and HAP (**Figure 5c** and Figure S2c) were not effective for the activation or monitoring of mtDNA damage.

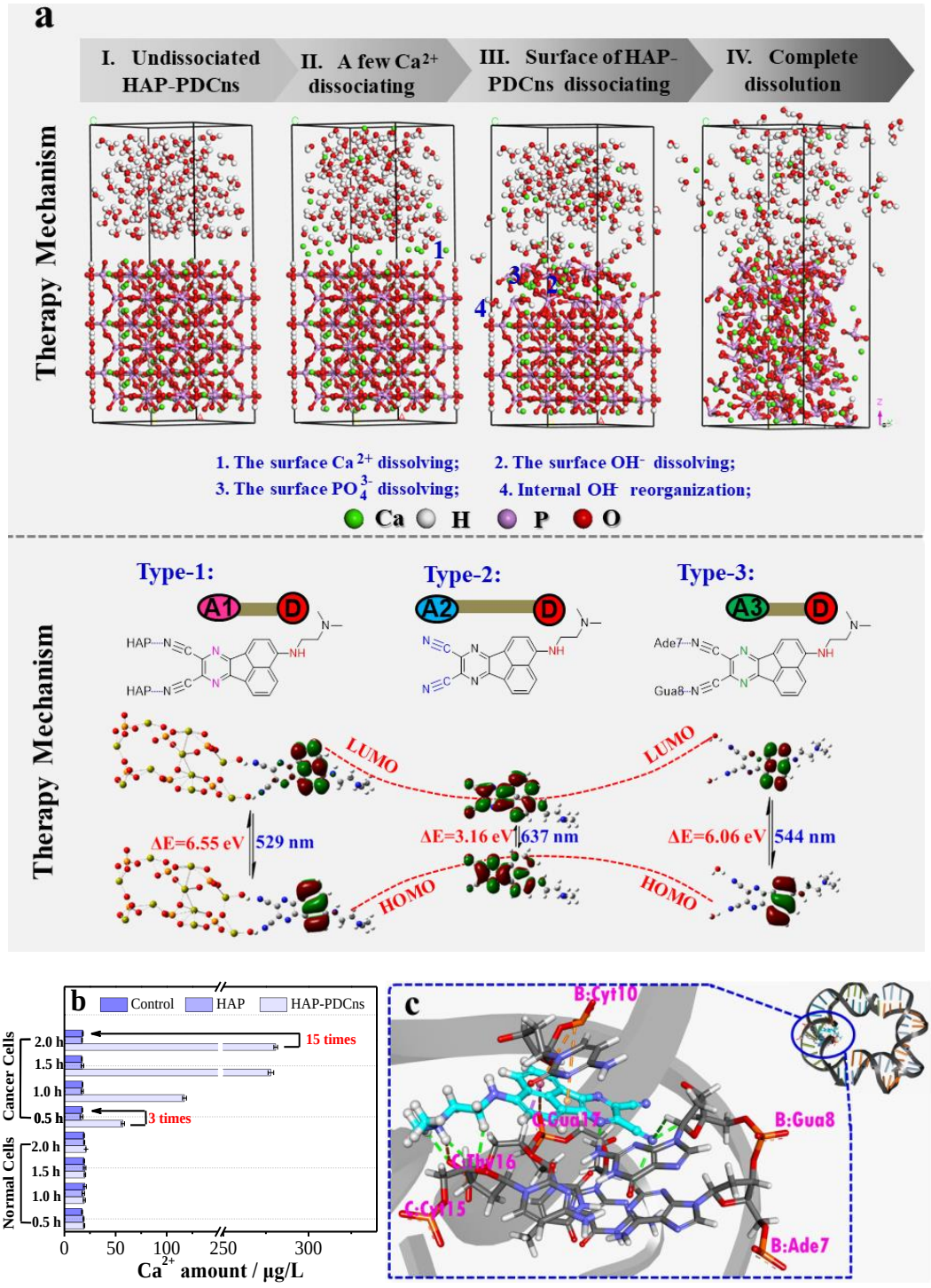

Figure 6. The activation and monitoring mechanism of **HAP-PDCns** for cancer cells. (a). Molecular dynamics calculations and quantitative theoretical calculation for different decomposition patterns of **HAP-PDCns**. (b).

The change in amounts of Ca^{2+} during the dissolution of **HAP-PDCns** using ICP-MASS. The experiments were performed in parallel three times. (c). The molecular docking of PDC to damage sites within mtDNA.

The activation and monitoring mechanism of **HAP-PDCns** for mtDNA damage of cancer cells is due mainly to the different decomposition patterns of **HAP-PDCns** in living systems. The amounts of Ca^{2+} were used to indicate the degree of decomposition of **HAP-PDCns**. The activation mechanism of **HAP-PDCns** was analyzed and verified using molecular dynamics (**Figure 6a)** and ICP-MASS (**Figure 6b**). Molecular dynamics data (**Figure 6a-I**) indicated that the structure of **HAP-PDCns** is stable and ordered. However, once **HAP-PDCns** enters into the dissolution process when it encounters mtDNA, the structure of **HAP-PDCns** (**Figure 6a** and avi-S1) and the amounts of Ca^{2+} (**Figure 6b**) undergo dramatic changes. **Figure 6b** indicates that the amount of Ca^{2+} in cancer cells is 3-times higher than normal cells and blank group when incubated with **HAP-PDCns** for 0.5 h. In other words, due to its microporous structures, **HAP-PDCns** instantly decomposes in the weakly acidic environment of the living cancer cells over the first half hour.[45,46] Molecular dynamics data (**Figure 6a-II** and avi-S1) verified this kind of decomposition, and indicated that this only happens on the surface of **HAP-PDCns**. Since surface Ca^{2+} are removed from **HAP-PDCns**, **HAP-PDCns** becomes negatively charged, which is why the system susequently locates in the mitochondria (**Figure 4a**). The dissolved Ca^{2+} is then released into the mitochondria of cancer cells, resulting in potential dissipation of the mitochondrial membrane (Figure S5) and damage of the mtDNA. Then the PDC units which are bound to the surface -OH groups of **HAP-PDCns** by a single hydrogen bond can easily leave the surface, and PDC can bind to the damage sites of mtDNA using seven hydrogen bonds and stacking interactions (**Figure 6c**, Green lines: hydrogen bonds; Orange lines: stacking interactions). The binding energy (-350.70 KJ/mol) of PDC with the damage sites of mtDNA was much lower than that of PDC with HAP

(*i.e.* **HAP-PDCns**, -328.57 KJ/mol). Molecular dynamics results (**Figure 6a-III**) indicated that superface OH^- and PO_4^{3-} groups of **HAP-PDCns** without protection by PDC completely dissociate into the aqueous environment of cancer cells (**Figure 6a-III**). The structure of **HAP-PDCns** becomes more and more open, and **HAP-PDCns** completely dissolves to form Ca^{2+}, OH^-, PO_4^{3-} and free PDC (**Figure 6a-IV**). ICP-MASS results (**Figure 6b**) indicated that the amount Ca^{2+} in the cancer cells at this stage increases to 277 μg/L, which is approximately 15-tmies higher than normal cells and control groups. Furthermore, different intracellular factors (such as, ionic strength, pH, temperature, and presence of proteins) were evaluated as possible activators for the release of Ca^{2+}. The test results indicate that the structural destruction of **HAP-PDCns** and the release of Ca^{2+} are triggered by protons (Figure S12). Therefore, producing an overload of Ca^{2+} in the cancer cells and resulting in mtDNA damage which triggers appoptosis and death of the cancer cells.

In addition, the monitoring mechanism of **HAP-PDCns** was analyzed and verified. The monitoring signal of **HAP-PDCns** is related to the PDC, and the changes of signal are mainly due to changes of the electron-withdrawing groups and the energy gap (*Δ*E) between HOMO and LUMO. When the **HAP-PDCns** enters the cell and has not dissolved, shown as Type-1 in **Figure 6a**, *i.e.* -the CN groups of the PDC unit interact with the -OH groups of the HAP unit through hydrogen bonds to form **HAP-PDCns** (**Scheme 1**). Calculation results (**Figure 6a**) predict a simulated emission wavelength of 529 nm, *i.e.* a green fluorescence signal, which was consistent with **Figure 2 I Process**. This is due to the -N- in the heterocycle as electron-withdrawing groups and -NH- as electron-donating group, producing an *Δ*E of 6.55 eV. Once the **HAP-PDCns** has decomposed, it can release PDC (Type-2 of **Figure 6a**) as an independent unit. The calculation results (**Figure 6a**) indicate that the electron-donating group does not change, but the electron-

withdrawing groups become -CN and the ΔE decreases to 3.16 eV, so the predicted emission wavelength red-shifts to 637 nm, *i.e.* a red fluorescence signal, which is consistent with **Figure 2 II** and **III** Process. Subsequently, PDC combines with damage sites in the mtDNA (**Figure 6c**) when the cancer cells are Ca^{2+} overloaded the -CN groups in the PDC are then bound with Ade7 and Gua8 of the mtDNA (**Figure 6c**), which result in a decrease of the electron-withdrawing ability of the -CN groups. The electron-withdrawing group returns to being the -N- in the heterocycle. **Figure 6a** indicates that the ΔE increases again up to 6.06 eV, and the predicted emission wavelength is blue-shifted to 544 nm, *i.e.* a green fluorescence signal, which is consistent with **Figure 2 IV** Process. Thus, a green-red-green monitoring signal is observed during the process of killing the cancer cells by **HAP-PDCns**, this is caused by switching of the electron-withdrawing groups and ΔE changes.

CONCLUSION

In summary, to facilitate the positive impact of mtDNA damage for living organisms, we have developed a proton-triggered decomposable hydroxyapatite ultrathin nanosheet (**HAP-PDCns**), which is a high Ca^{2+} content biomaterial. **HAP-PDCns** made up of two key components, pyrazine-2,3-dicarbonitrile (PDC) and hydroxyapatite (HAP). The two key components were hybridized to form the loose **HAP-PDCns** material held together by hydrogen bonds, enabling triggered destruction through dissolution. In the free state, **HAP-PDCns** is a stable green fluorescence emitter at 529 nm. When the structure of **HAP-PDCns** collapses to release Ca^{2+} and to facilitate Ca^{2+}overload, in the mitochondria of cancer cells a red fluorescence signal at 637 nm emerges. Finally, mtDNA develops many damage sites because of calcium overload, and a green fluorescence signal at 544 nm re-emerges. As such **HAP-PDCns** has many clear advantages for

living systems, which are, activation and monitoring of mtDNA damage and triggering the apoptosis and death of cancer cells. The biological experiments, quantitative theoretical calculations and molecular dynamics simulations verified that the mechanism of **HAP-PDCns** induced mtDNA damage was triggered by the destruction of the loose structure containing PDC. The monitoring mechanism of **HAP-PDCns** for mtDNA damage was shown to be the switching of electron-withdrawing groups and ΔE changes between the HOMO and LUMO. Overall, the main advantages of our system are the triggered destruction of nanoparticles that can activate mtDNA damage in cancer cells resulting in significant positive impacts for the living organism, including: (1) mtDNA damage specifically in cancer cells; (2) generation of multiple output/monitoring signals; (3) triggered and controllable destruction of the nanoparticles. Based on our design strategy, we anticipate that many other groups will work towards the design and development of nanoparticles possessing triggered destructive capabilities in order to activate similar positive outcomes for living organisms.

EXPERIMENTAL SECTION

Synthesis of PDC. 5-bromoacenaphthylene-1, 2-dione (1.0 mmol, 560 mg)) and diaminomaleonitrile (2.0 mmol, 464 mg) were stirred in acetic acid solution for 2 h at 110^{o}C. Then the solvent was evaporated by vacuum distillation and the residue was purified by column chromatography on silica gel eluted with CH_2Cl_2 to obtain 3-bromoacenaphtho[1, 2-b]pyrazine-8,9-dicarbonitrile. Next, 3-bromoacenaphtho[1, 2-b]pyrazine-8,9-dicarbonitrile (1.0 mmol, 450 mg) and N,N-dimethyl-1, 2-ethylenediamine (5.0 mmol, 727 μL) were stirred in 20 mL 2-methoxyethanol for 4 h at 110^{o}C. Then, the solution was poured into ice water and the precipitate

was filtered, and the solid was purified by column chromatography on silica gel eluted with CH_2Cl_2/CH_3OH (50:3 to 50:2, v/v) to obtain PDC. Yield 55 %. ^1H NMR (600 MHz, $CDCl_3$) δ 8.45 (d, 1H, J = 4.6 Hz), 8.29 (d, 1H, J = 5.3 Hz), 8.25 (d, 1H, J = 5.3 Hz), 7.84 (t, 1H, J = 4.9 Hz), 6.83 (s, 1H), 6.77 (d, 1H, J = 5.4 Hz), 3.52 (d, 2H, J = 2.3 Hz), 2.81 (t, 2H, J = 3.4 Hz), 2.39 (s, 6H). ^{13}C NMR (151 MHz, $CDCl_3$) δ 151.16, 150.62, 150.08, 135.88, 129.28, 128.42, 126.54, 125.38, 124.77, 124.61, 124.41, 118.04, 114.07, 113.78, 113.73, 105.98, 55.78, 44.02, 39.07. HRMS (ESI) m/z: $[M + H]^+$ calcd for $C_{20}H_{16}N_6$, 341.1470; found, 341.1503.

Synthesis of HAP-PDC. Calcium nitrate (0.40 mmol) was dissolved in a round bottom flask containing 3 mL of doubly purified water, adding 2 mL anhydrous ethanol solution of the PDC, and then stir for 6 h in the dark. After that 5 mL dipotassium hydrogen phosphate (0.27 mmol) solution was added, and the solution pH was adjusted to 7.4 with the dilute ammonia water. The mixture was then stirred for 72 h at 37ºC. Then the reaction mixture centrifuged and washed with anhydrous ethanol several times to remove excess dye.

Characterization. The NMR spectra of PDC were obtained using Avance 600 MHz spectrometers (Bruker Co., Switzerland). The size and morphology of **HAP-PDCns** was characterized using High-Resolution Transmission Electron Microscope (HR-TEM, JEM-2100, JEOL), Field-Emission Scanning Electron Microscope (FE-SEM, Hitachi S4800), X-ray diffraction spectrum (XRD, Bruker axs Com.) and Fourier Transform Infrared Spectrometer (FT-IR, Perkin-Elmer Spectrum 400F). The Fluoromax-4 spectrophotometer (HORIBA-PLUS-C) was used to measure the fluorescence spectra.

The evaluation of HAP-PDCns with cancer cells. Inhibition by **HAP-PDCns** was characterized by the mitochondrial membrane potential assay and the cellular apoptosis and death assay. After incubation with PDC (5.0 μM), **HAP-PDCns** (0.40 mg/mL, 1.2 mg/mL) and HAP

(0.40 mg/mL). The mitochondrial membrane potential were determined by flow cytometry after adding JC-1. The cellular apoptosis and death assay were determined by flow cytometry after staining with Annexin V-FITC and PI. The inhibition abilities of **HAP-PDCns** for cancer cell proliferation was determined by MTT assay.

Evaluation of the monitoring ability of HAP-PDCns for mtDNA damage. HepG 2 cell lines and AML12 cell lines were incubated with 0.40 mg/mL of **HAP-PDCns** for different times(0.5 h, 1.0 h, 1.5 h and 2.0 h). Then, fluorescence images were obtained using FV10-ASW.

The inhibition of HAP-PDCns on tumor development. The inhibition effects were verified *in vivo.* Tumor-bearing (S180 cell line) BALB/c mice were continuously injected with **HAP-PDCns** (0.40 mg/mL and 0.0004 mg/mL), HAP (0.40 mg/mL) and PDC (5.0 μM) for 15 d, respectively. The results were obtained by the visual images of tumor volume change and the value of tumor volume change.

Clinicopathology. After the tumors were injected by PDC (5.0 μM), **HAP-PDCns** (0.40 mg/mL) and HAP (0.40 mg/mL), and fixed with 4% formaldehyde. The tumors were then cut into thin slices, and stained usig hematoxylin and eosin (H&E).

The activation and monitoring mechanism of HAP-PDCns for mtDNA damage of cancer cells. The therapy mechanism of **HAP-PDCns** was analyzed and verified using molecular dynamics and ICP-MASS. In short, HepG 2 cell lines and AML12 cell lines were incubated with 0.40 mg/mL of **HAP-PDCns** for different times(0.5 h, 1.0 h, 1.5 h and 2.0 h). The cells were collected and centrifuged, then the change in amounts of calcium ions at different times were quantified by ICP-MASS. The molecular dynamics calculations of **HAP-PDCns** were performed using the discover module of Materials Studio software. The monitoring mechanism of **HAP-**

PDCns was analyzed and verified using quantitative theoretical calculation using the Gaussian 16 suite.

ASSOCIATED CONTENT

Supporting Information.

Supporting Information is available from the ACS Publication website.

Supporting Information (PDF); Molecular dynamic calculations for the different decomposition patterns of HAP-PDCns (AVI)

AUTHOR INFORMATION

Corresponding Author

email: zhanghua1106@163.com

Author Contributions

The manuscript was written through contributions of all authors. All authors have given approval to the final version of the manuscript. ‡These authors contributed equally. (match statement to author names with a symbol)

Notes

The authors declare no competing interests.

ACKNOWLEDGMENT

This work was supported by the National Natural Science Foundation of China (21722501, 22004028 and 11974103). H. Zhang wishes to thank the zhongyuan high level talents special

support plan—Science and Technology Innovation Leading Talents (204200510006). The High Performance Computing Center of Henan Normal University. T. D. James wishes to thank the Royal Society for a Wolfson Research Merit Award.

REFERENCES

(1) Mckee, T.; Me Mckee J. R. *Biochemistry: an introduction (Second Edition)*. McGraw-Hill Companies, Inc. **1999**, pp 459-525.

(2) Ishikawa, K.; Takenaga, K.; Akimoto, M.; Koshikawa, N.; Yamaguchi, A.; Imanishi, H.; Nakada, K.; Honma, Y.; Hayashi, J. I. ROS-Generating Mitochondrial DNA Mutations can Regulate Tumor Cell Metastasis. *Science* **2008**, *320* , 661-664.

(3) McArthur, K.; Whitehead, L. W.; Heddleston, J. M.; Li, L.; Padman, B. S.; Oorschot, V.; Geoghegan, N. D.; Chappaz, S.; Davidson, S.; San Chin, H.; Lane, R. M.; Dramicanin, M.; Saunders, T. L.; Sugiana, C.; Lessene, R.; Osellame, L. D.; Chew, T. L.; Dewson, G.; Lazarou, M.; Ramm, G.; Lessene, G.; Ryan, M. T.; Rogers, K. L.; van Delft, M. F.; Kile, B. T. BAK/BAX Macropores Facilitate Mitochondrial Herniation and mtDNA Efflux During Apoptosis. *Science* **2018**, *359*, eaao6047.

(4) Higurashi, M.; Maruyama, T.; Nogami, Y.; Ishikawa, F.; Yoshida, Y.; Mori, K.; Fujita, K. I.; Shibanuma, M. High Expression of FOXM1 Critical for Sustaining Cell Proliferation in Mitochondrial DNA-Less Liver Cancer Cells. *Exp. Cell Res.* **2020**, *389*, 111889.

(5) Santos, J. H.; Meyer, J. N.; Van Houten, B. Mitochondrial Localization of Telomerase as a Determinant for Hydrogen Peroxide-Induced Mitochondrial DNA Damage and Apoptosis. *Hum. Mol. Genet.* **2006**, *15*, 1757-1768.

(6) Tahbaz, N.; Subedi, S.; Weinfeld, M. Role of Polynucleotide Kinase/Phosphatase in Mitochondrial DNA Repair. *Nucleic Acids Res.* **2012**, *40*, 3484-3495.

(7) Sharma, P.; Sampath, H. Mitochondrial DNA Integrity: Role in Health and Disease. *Cells* **2019**, *8*, 100.

(8) Bender, A.; Krishnan, K. J.; Morris, C. M.; Taylor, G. A.; Reeve, A. K.; Perry, R. H.; Jaros, E.; Hersheson, J. S.; Betts, J.; Klopstock, T.; Taylor, R. W.; Turnbull, D. M. High Levels of Mitochondrial DNA Deletions in Substantia Nigra Neurons in Aging and Parkinson Disease. *Nat. Genet.* **2006**, *38*, 515-517.

(9) Rebbeck, C. A.; Leroi, A. M.; Burt, A. Mitochondrial Capture by a Transmissible Cancer. *Science* **2011**, *331*, 303.

(10) Mirza-Aghazadeh-Attari, M.; Ostadian, C.; Saei, A. A.; Mihanfar, A.; Darband, S. G.; Sadighparvar, S.; Kaviani, M.; Samadi Kafil, H.; Yousefi, B.; Majidinia, M. DNA Damage Response and Repair in Ovarian Cancer: Potential Targets for Therapeutic Strategies. *DNA Repair* **2019**, *80*, 59-84.

(11) Wang, H.; Xiang, D. X.; Liu, B.; He, A.; Randle, H. J.; Zhang, K. X.; Dongre, A.; Sachs, N.; Clark, A. P.; Tao, L. W.; Chen, Q.; Botchkarev, V. V., Jr.; Xie, Y.; Dai, N.; Clevers, H.; Li, Z.; Livingston, D. M. Inadequate DNA Damage Repair Promotes Mammary Transdifferentiation, Leading to BRCA1 Breast Cancer. *Cell* **2019**, *178*, 135-151.

(12) Kang, E.; Wu, J.; Gutierrez, N. M.; Koski, A.; Tippner-Hedges, R.; Agaronyan, K.; Platero-Luengo, A.; Martinez-Redondo, P.; Ma, H.; Lee, Y. Mitochondrial Replacement in Human Oocytes Carrying Pathogenic Mitochondrial DNA Mutations. *Nature* **2016**, *540*, 270-275.

(13) Wang, Y. F.; An, R.; Umanah, G. K.; Park, H.; Nambiar, K.; Eacker, S. M.; Kim, B.; Bao, L.; Harraz, M. M.; Chang, C.; Chen, R.; Wang, J. E.; Kam, T. I.; Seop Jeong, J.; Xie, Z.; Neifert, S.; Qian, J.; Andrabi, S. A.; Blackshaw, S.; Zhu, H.; Song, H. J.; Ming, G. L.; Dawson, V. L.; Dawson,

T. M. A Nuclease that Mediates Cell Death Induced by DNA Damage and Poly(ADP-Ribose) Polymerase-1. *Science* **2016**, *354*, 82.

(14) Kuo, C. H.; Leu, Y. L.; Wang, T. H.; Tseng, W. C.; Feng, C. H.; Wang, S. H.; Chen, C. C. A Novel DNA Repair Inhibitor, Diallyl Disulfide (DADS), Impairs DNA Resection During DNA Double-Strand Break Repair by Reducing Sae2 and Exo1 Levels. *DNA Repair* **2019**, *82*, 102690.

(15) Zhang, Y.; Hua, R. N.; Xiang, D. X.; Zhang, C. Y. Single-Molecule Counting of Oxidative DNA Damage in Telomeres from Cancer Cells. *Chem. Commun.* **2019**, *55*, 7627-7630.

(16) Jiang, W.; Li, Q.; Zhu, Z. C.; Wang, Q.; Dou, J. X.; Zhao, Y. M.; Lv, W. F.; Zhong, F.; Yao, Y. D.; Zhang, G. Q.; Liu, H.; Wang, Y. C.; Wang, J. Cancer Chemoradiotherapy Duo: Nano-Enabled Targeting of DNA Lesion Formation and DNA Damage Response. *ACS Appl. Mater. Interfaces* **2018**, *10*, 35734-35744.

(17) Miao, Q. Q.; Xie, C.; Zhen, X.; Lyu, Y.; Duan, H. W.; Liu, X. G.; Jokerst, J. V.; Pu, K. Y. Molecular Afterglow Imaging with Bright, Biodegradable Polymer Nanoparticles. *Nat. Biotech.* **2017**, *35*, 1102-1110.

(18) Li, Q.; Li, S. H.; He, S. S.; Chen, W.; Cheng, P. H.; Zhang, Y.; Miao, Q. Q.; Pu, K. Y. An Activatable Polymeric Reporter For Near-Infrared Fluorescent and Photoacoustic Imaging of Invasive Cancer. *Angew. Chem. Int. Edit.* **2020**, *59*, 7018-7023.

(19) Li, J. C.; Pu, K. Y. Development of Organic Semiconducting Materials for Deep-Tissue Optical Imaging, Phototherapy and Photoactivation. *Chem. Soc. Rev.* **2019**, *48*, 38-71.

(20) Zhang,Y.; Xu, C.; Yang, X. L.; Pu, K. Y. Photoactivatable Protherapeutic Nanomedicine for Cancer. *Adv. Mater.* **2020**, *32*, 2002661.

(21) Li, J. C.; Pu, K. Y. Semiconducting Polymer Nanomaterials as Near-Infrared Photoactivatable Protherapeutics for Cancer. *Acc. Chem. Res.* **2020**, *53*, 752-762.(22) Cheng, P. H.; Pu, K. Y.

Activatable Phototheranostic Materials for Imaging-Guided Cancer Therapy. *ACS Appl. Mater. Interfaces* **2020**, *12*, 5286-5299.

(23) Li, J. C.; Cui, D.; Jiang, Y. Y.; Huang, J. G.; Cheng, P. H.; Pu, K. Y. Near-Infrared Photoactivatable Semiconducting Polymer Nanoblockaders for Metastasis-Inhibited Combination Cancer Therapy. *Adv. Mater.* **2019**, *31*, 1905091.

(24) Tian, B.; Li, J. L.; Pang, R. J.; Dai, S.; Li, T.; Weng, Y. L.; Jin, Y.; Hua, Y. J. Gold Nanoparticles Biosynthesized and Functionalized Using a Hydroxylated Tetraterpenoid Trigger Gene Expression Changes and Apoptosis in Cancer Cells. *ACS Appl. Mater. Interfaces* **2018**, *10*, 37353-37363.

(25) Jiang, W.; Li, Q.; Xiao, L.; Dou, J. X.; Liu, Y.; Yu, W. H.; Ma, Y. C.; Li, X. Q.; You, Y. Z.; Tong, Z. T.; Liu, H.; Liang, H.; Lu, L. G.; Xu, X. D.; Yao, Y. D.; Zhang, G. Q.; Wang, Y. C.; Wang, J. Hierarchical Multiplexing Nanodroplets for Imaging-Guided Cancer Radiotherapy via DNA Damage Enhancement and Concomitant DNA Repair Prevention. *ACS Nano* **2018**, *12*, 5684-5698.

(26) Wen, L.; Chen, L.; Zheng, S. M.; Zeng, J. F.; Duan, G. X.; Wang, Y.; Wang, G. L.; Chai, Z. F.; Li, Z.; Gao, M. Y. Ultrasmall Biocompatible WO_{3-x} Nanodots for Multi-Modality Imaging and Combined Therapy of Cancers. *Adv. Mater.* **2016**, *28*, 5072-5079.

(27) Zhang, X. D.; Chen, J.; Min, Y.; Park, G. B.; Shen, X.; Song, S. S.; Sun, Y. M.; Wang, H.; Long, W.; Xie, J. P.; Gao, K.; Zhang, L. F.; Fan, S. J.; Fan, F. Y.; Jeong, U. Metabolizable Bi_2Se_3 Nanoplates: Biodistribution, Toxicity, and Uses for Cancer Radiation Therapy and Imaging. *Adv. Funct. Mater.* **2014**, *24*, 1718-1729.

(28) Li, X. Z.; Wu, J. G.; He, C.; Chen, L. Y.; Jiao, Y.; Duan, C. Y.; Wang, L. Mitochondrial DNA-Targeted Ir(III)-Containing Metallohelices with Tunable Photodynamic Therapy Efficacy in Cancer Cells. *Angew. Chem. Int. Edit.* **2020**, *59*, 6420-6427.

(29) Niemeyer, C. M. Nanoparticles, Proteins, and Nucleic Acids: Biotechnology Meets Materials Science. *Angew. Chem. Int. Edit.* **2001**, *40*, 4128-4158.

(30) Shi, D. L. Integrated Multifunctional Nanosystems for Medical Diagnosis and Treatment. *Adv. Funct. Mater.* **2009**, *19*, 3356-3373.

(31) Sun, T. M.; Zhang, Y. S.; Pang, B.; Hyun, D. C.; Yang, M. X.; Xia, Y. N. Engineered Nanoparticles for Drug Delivery in Cancer Therapy. *Angew. Chem. Int. Edit.* **2014**, *53*, 12320-12364.

(32) Hou, C. H.; Hou, S. M.; Hsueh, Y. S.; Lin, J.; Wu, H. C.; Lin, F. H. The in Vivo Performance of Biomagnetic Hydroxyapatite Nanoparticles in Cancer Hyperthermia Therapy. *Biomaterials* **2009**, *30*, 3956-3960.

(33) Li, X. Y.; Zou, Q.; Li, W.; Chen, H. F. Intracellular Interaction of Hydroxyapatite-Based Nanocrystals with Uniform Shape and Traceable Fluorescence. *Inorg. Chem.* **2018**, *57*, 13739-13748.

(34) Kapat, K.; Shubhra, Q. T. H.; Zhou, M.; Leeuwenburgh, S. Piezoelectric Nano-Biomaterials for Biomedicine and Tissue Regeneration. *Adv. Funct. Mater.* **2020**, *30*, 1909045.

(35) Xue, S. F.; Chen, Z. H.; Han, X. Y.; Lin, Z. Y.; Wang, Q. X.; Zhang, M.; Shi, G. DNA Encountering Terbium (III): A Smart "Chemical Nose/Tongue" for Large-Scale Time-Gated Luminescent and Lifetime-Based Sensing. *Anal. Chem.* **2018**, *90*, 3443-3451.

(36) Xiong, H.; Zuo, H.; Yan, Y. F.; Occhialini, G.; Zhou, K. J.; Wan, Y. H.; Siegwart, D. J. High-Contrast Fluorescence Detection of Metastatic Breast Cancer Including Bone and Liver

Micrometastases via Size-Controlled pH-Activatable Water-Soluble Probes. *Adv. Mater.* **2017**, *29*, 1700131.

(37) Hao, M.; He, J. L.; Wang, C. H.; Wang, C.; Ma, B. J.; Zhang, S.; Duan, J. Z.; Liu, F.; Zhang, Y.; Han, L.; Liu, H.; Sang, Y. H. Effect of Hydroxyapatite Nanorods on the Fate of Human Adipose-Derived Stem Cells Assessed In Situ at the Single Cell Level with a High-Throughput, Real-Time Microfluidic Chip. *Small* **2019**, *15*, 1905001.

(38) Kowada, T.; Kikuta, J.; Kubo, A.; Ishii, M.; Maeda, H.; Mizukami, S.; Kikuchi, K. In Vivo Fluorescence Imaging of Bone-Resorbing Osteoclasts. *J. Am. Chem. Soc.* **2011**, *133*, 17772-17776.

(39) Neacsu, I. A.; Stoica, A. E.; Vasile, B. S.; Andronescu, E. Luminescent Hydroxyapatite Doped with Rare Earth Elements for Biomedical Applications. *Nanomaterials* **2019**, *9*, 239.

(40) Mercer, J.; Schelhaas, M.; Helenius, A. Virus Entry by Endocytosis. *Annu. Rev. Biochem.* **2010**, *79*, 803-833.

(41) von Kleist, L.; Stahlschmidt, W.; Bulut, H.; Gromova, K.; Puchkov, D.; Robertson, M. J.; MacGregor, K. A.; Tomilin, N.; Pechstein, A.; Chau, N.; Chircop, M.; Sakoff, J.; von Kries, J. P.; Saenger, W.; Kräusslich, H. G.; Shupliakov, O.; Robinson, P. J.; McCluskey, A.; Haucke1, V. Role of the Clathrin Terminal Domain in Regulating Coated Pit Dynamics Revealed by Small Molecule Inhibition. *Cell* **2011**, *146*, 471-484.

(42) Zheng, X. P.; Liu, Y.; Yang, Y. M.; Wei, D.; Xu, Y. Y.; Wei, Q.; Du, B. Synthesis of Hydroxyapatite in Microemulsion and its Adsorption Properties for Human Serum Albumin. *Adv. Mater. Res.* **2009**, *79-82*, 51-54.

(43) Koide, R.; Nishimura, S. I. Antiadhesive Nanosomes Facilitate Targeting of the Lysosomal GlcNAc Salvage Pathway through Derailed Cancer Endocytosis. *Angew. Chem. Int. Edit*. **2019**, *58*, 14513-14518.

(44) Pinho, S. S.; Reis, C. A. Glycosylation in Cancer: Mechanisms and Clinical Implications. *Nat. Rev. Cancer* **2015**, *15*, 540-555.

(45) Huang, C. C.; Chia, W. T.; Chung, M. F.; Lin, K. J.; Hsiao, C. W.; Jin, C.; Lim, W. H.; Chen, C. C.; Sung, H. W. An Implantable Depot that Can Generate Oxygen In Situ for Overcoming Hypoxia-Induced Resistance to Anticancer Drugs in Chemotherapy. *J. Am. Chem. Soc.* **2016**, *138*, 5222-5225.

(46) Beck, B.; Blanpain, C. Unravelling Cancer Stem Cell Potential. *Nat. Rev. Cancer* **2013**, *13*, 727-738.